

Supporting Information to:

Single-Molecule Electrocatalysis by Single-Walled Carbon Nanotubes

Weilin Xu, Hao Shen, Yoon Ji Kim, Xiaochun Zhou, Guokun Liu, Jiwoong Park, and Peng Chen*

Department of Chemistry and Chemical Biology, Cornell University, Ithaca, NY 14853, U.S.A.

E-mail: pc252@cornell.edu

I. Experimental Methods

I.1. Purification of SWNTs. The single-walled carbon nanotubes were purchased from Carbon Nanotechnologies Incorporated (Purified HiPCO single-walled carbon nanotubes). These SWNTs have an average diameter of 1 ± 0.3 nm and typically microns long.¹ We further purified the SWNTs by refluxing them in 70% HNO₃ solution at 60-80°C for 24 hours to reduce the amount of residual metal catalysts.² The acid-treated SWNT suspensions were then centrifuged at variable speeds to remove amorphous carbon and carbon nanoparticles according to the literature procedures.³

I.2. Ensemble electrochemistry. Ensemble electrochemistry were performed using an electrochemical analyzer (CHI1200A, CH Instruments, Inc.) with three electrode system. A Ag/AgCl (KCl saturated) was used as the reference electrode and a Pt foil was used as the counter electrode. The working electrode was glassy carbon, ITO (Delta Technologies, LTD), ITO-supported SWNTs, or ITO-supported carbon black. To prepare SWNT or carbon black coated ITO, a slurry was first prepared by sonicating 5 mg of SWNTs or carbon black, and 50 μ L of Nafion solution (Aldrich, 5% wt Nafion) in 1 mL ethanol for 30-minute. 20 μ L of the slurry was then spread on the ITO surface and dried. The support electrolyte is 50 mM phosphate buffer at pH 7.3.

I.3. Single-molecule fluorescence microscopy. Single-molecule fluorescence measurements were performed on a homebuilt prism-type total internal reflection (TIR) fluorescence microscope based on an Olympus IX71 inverted microscope. A continuous wave circularly polarized 532 nm laser beam (CrystaLaser, GCL-025-L-0.5%) of 3-6 mW was focused onto an area of $\sim 90 \times 45$ μ m² on the sample to directly excite the fluorescence of resorufin. The fluorescence of resorufin was collected by a 60X NA1.2 water-immersion objective (UPLSAPO60XW, Olympus), optically filtered (HQ550LP) to reject laser scattering, and projected onto a camera (Andor iXon EMCCD, DV887DCS-BV), which is controlled by an Andor IQ software and operated at up to 30-ms frame rate. Sometimes an additional filter (HQ580m60) was also used in the detection path. All optical filters are from Chroma Technology Corp. All experiments were done at room temperature. The movies are analyzed using a home-written IDL program, which extracts the fluorescence intensity trajectories from localized fluorescence spots

individually across the entire movie. The intensity of each bright spot in an image is obtained by integrating the signal counts over an area of $\sim 1 \times 1 \mu\text{m}^2$.

I.4. Electrochemical flow cell preparation. A flow cell (height \times length \times width = $100 \mu\text{m} \times 2 \text{cm} \times 5 \text{mm}$), formed by double-sided tapes sandwiched between a glass slide and a borosilicate coverslip (Gold Seal[®]), was used to hold aqueous sample solutions for single-molecule fluorescence measurements. Part of the glass slide was cut to inset an ITO-coated quartz slide. Before assembled into a flow cell, $20 \mu\text{L}$ of SWNT suspension (1% w.t.), which was purified and sonicated for an hour, was deposited on the ITO-coated quartz slide and incubated for 30 minutes; the slide was then rinsed for 3 minutes with MilliQ water to wash away unbound SWNTs. On the quartz slide, three holes were drilled. Two of them were used to connect to polyethylene tubing and a syringe pump for continuous solution flow at $15 \mu\text{L}/\text{minute}$. The third one was used to place the Ag/AgCl reference electrode. A Pt foil was sandwiched between the coverslip and the quartz slide as counter electrode; care was taken to avoid contact between the Pt foil and the ITO surface to prevent short circuit.

I.5. Super-resolution imaging analysis. Our image analysis for single-molecule super-resolution optical imaging largely follows the procedures as in STORM^{4,5} with slight modifications. Specifically, to determine the center of the emission point spread function (PSF) of a single **P** molecule at a reactive site, an image area of 13×13 pixels ($\sim 3.5 \times 3.5 \mu\text{m}^2$) around the molecule were used for two-dimensional Gaussian fitting. For each **P** molecule detected during a τ_{on} period, all image frames during an entire τ_{on} period were combined to form a single image to have a large number of fluorescence photons for the analysis. Because the camera chip consists of square pixels of finite size, to improve fitting accuracy, the image is fitted to:

$$I(x, y) = A + Bx + Cy + \int_{x-\delta}^{x+\delta} \int_{y-\delta}^{y+\delta} dx dy I_0 \exp \left[-\frac{1}{2} \left(\frac{x-x_0}{\sigma_x} \right)^2 - \frac{1}{2} \left(\frac{y-y_0}{\sigma_y} \right)^2 \right]$$

Here $I(x, y)$ is the intensity counts of the fluorescent molecule in the image at position

(x, y) , $I_0 \exp \left[-\frac{1}{2} \left(\frac{x-x_0}{\sigma_x} \right)^2 - \frac{1}{2} \left(\frac{y-y_0}{\sigma_y} \right)^2 \right]$ is a two-dimensional Gaussian function, and δ is

half of the pixel size. Along x or y axis, the integration over each pixel is done numerically by dividing each pixel into 11 equal segments (further increasing the number of segments does not improve the fitting accuracy). Because the laser excitation in our experiment is not homogeneous over the entire illumination area (note the area analyzed for one molecule is very small relative to the laser beam size though), we used a sloping plane $A+Bx+Cy$ to account for the background in the fitting. (x_0, y_0) gives the center location of the PSF.

The accuracy of the center localization was determined according to Thompson et al.⁵⁻⁷

$$Er_i = \sqrt{\frac{\sigma_i^2}{N} + \frac{a^2}{12N} + \frac{8\pi\sigma_i^4 b^2}{a^2 N^2}}$$

Here Er_i ($i = x$ or y) is the x or y accuracy of the center location of the PSF, σ_i is from the two-dimensional Gaussian fitting of the emission PSF, N is the total number of fluorescence photons detected, a is the pixel size in the fluorescence image, and b is the standard deviation of the background. Provided large number of fluorescence photons are detected, Er_i can be as small as 1-2 nm.⁷ In our single-molecule electrocatalysis experiments, some τ_{on} periods are very short (Figure 2C), giving insufficient photon counts to achieve accurate localizations of the PSF. Therefore, localizations that have accuracy worse than ± 6 nm because of insufficient photon counts were filtered out, as similarly employed in STORM imaging.⁵

To obtain N , the number of photons detected for each molecule, the total integrated signal counts under the fitted two-dimensional Gaussian function is converted to the photon counts, according to the formula provided by the camera supplier (Andor Technology):

$$E_V = (\text{cts} / g) * (S / \text{QE}) * 3.65$$

Here E_V is the total energy of photons, cts is the counts from the EMCCD camera (unitless), g is EM gain (unitless), S is CCD sensitivity (electrons per count) and available from the EMCCD camera specification, QE is the quantum efficiency (unitless) of the camera in the spectral region of the detected fluorescence, and 3.65 is a physical constant for electron creation in Silicon (eV per electron). The total number of the photons, N , equals the total energy of photons E_V divided by the energy of a single photon, for which the center wavelength of the detected spectral region is used.

To obtain b , the standard deviation of the background, we first obtain the background image by subtracting the fitted 2-D Gaussian function from the original data image. Then we convert the counts in the background image to the number of photons before calculating the standard deviation of the background signal, i.e., b .

I.6. Other methods. Ensemble fluorescence measurements were performed using an Agilent Eclipse fluorometer at room temperature. Atomic force microscopy (Digital Instruments, Santa Barbara, CA) was done in tapping mode. SEM measurements were performed on a LEICA 440 SEM at the Cornell Center for Materials Research.

II. Additional Results and Analyses

II.1. Cyclic voltammetry of resazurin on SWNTs-coated ITO.

The cyclic voltammograms of resazurin using SWNTs-coated ITO as the working electrode at variable scan rates show two reduction peaks and one oxidation peak (Figure S1), attributable to **S** \rightarrow **P** reduction, **P** \rightarrow **PH₂** reduction, and **PH₂** \rightarrow **P** oxidation, respectively, as discussed in the text.

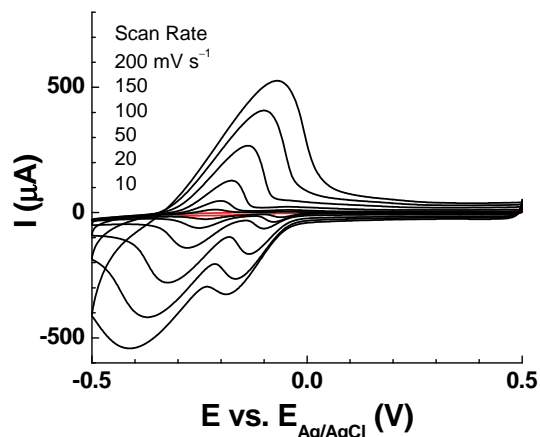


Figure S1. Cyclic voltammograms of 50 μM resazurin in 50 mM pH 7.3 phosphate solution using SWNT-coated ITO electrode at variable scan rates. The red curve is the background scan in the absence of resazurin at the lowest scan rate 10 mV s^{-1} .

II.2. Confirmation of resorufin formation after repeated cyclic voltammetry.

To further confirm the observed redox chemistry in the CV of resazurin using SWNTs-coated ITO as working electrode, we measured the fluorescence spectra of the reaction solution after repeated cycles of CV scans. With increasing number of CV scans, the intensity of the fluorescence band of resorufin increases (Figure S2), indicating the accumulation of resorufin, consistent with the expected redox chemistry (Figure 1A).

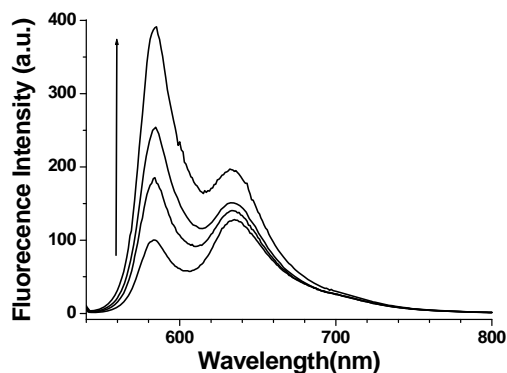


Figure S2. Fluorescence spectra of the reaction solution after repeated cyclic voltammetry scans of 6 μM resazurin in pH 7.3 phosphate buffer. Each fluorescence spectrum was taken after 10 cycles of cyclic voltammetry from 0.5 V to -0.5 V. The 585-nm band is from the fluorescence of resorufin. The ~ 635 -nm band is from the residual fluorescence of resazurin. (Note here resazurin is at much higher concentration than resorufin in the solution). The bottom spectrum is from the starting solution, and the 585-nm band intensity here reflects the 1% resorufin contained in the resazurin sample.⁸

II.3. Control experiments of SWNTs electrochemistry

Control experiments further support that SWNTs are responsible for the observed electrocatalysis of resazurin redox: (1) No appreciable redox is observed by CV in the same potential range in the absence of resazurin or SWNTs (Figure S3). (2) Purified SWNTs have higher electrocatalytic activity; thus the observed electrocatalysis is not due to impurities in the SWNTs (Figure S4C). (3) Iron or copper nanoparticles, two possible metal nanoparticle impurities in the SWNT sample, do not have electrocatalytic activity in resazurin reduction (Figure S5) (4) Possible amorphous carbon impurities cannot be the main contributor to the observed electrocatalytic activity (Figure S6).

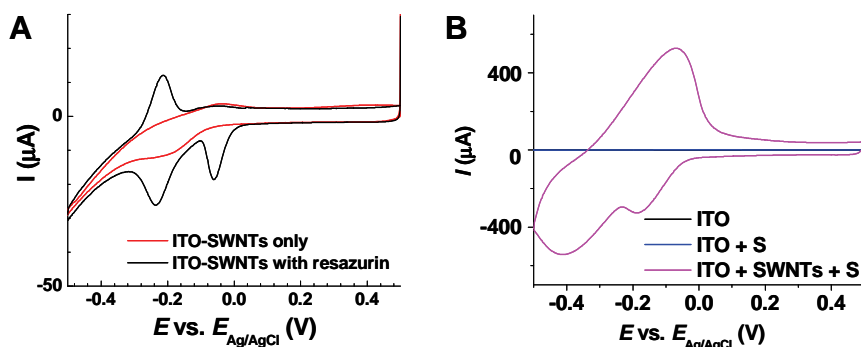


Figure S3. (A) Cyclic voltammogram of 50 μM resazurin in 50 mM pH 7.3 phosphate buffer using SWNTs-coated ITO as the working electrode at the scan rate of 10 mV s^{-1} (black line), in comparison with that in the absence of resazurin. (B) Comparison of CVs of resazurin in the presence and absence of SWNTs on the ITO electrode at the scan rate of 200 mV s^{-1} .

II.4. Comparison of electrocatalytic activity of purified and non-purified SWNTs.

We further purified the commercially obtained SWNTs using HNO_3 treatments to remove metal nanoparticle catalysts² and using centrifugation to remove amorphous carbon and carbon particles³ (see Experimental Methods above). Elemental analysis via energy dispersive x-ray spectroscopy (EDX) identified Fe as the only significant metal residual in the original SWNT sample, with $5.1 \pm 0.4\%$ atom percentage (Figure S4A). The purification process reduces the Fe residual to $1.9 \pm 0.4\%$ atom percentage (Figure S4A). The incomplete removal of metal catalysts is consistent with literature reports.⁹

The absorption spectra of the SWNTs indicate that the purification process also preferentially reduces the amount of metallic SWNTs in the sample relative to that of the semiconducting SWNTs, as the absorption features of metallic SWNTs in the $\sim 400\text{-}650 \text{ nm}$ region diminish relatively to those of semiconducting ones in the $\sim 650\text{-}1000 \text{ nm}$ region after purification (Figure S4B).¹⁰ This preferential removal of metallic SWNTs is due to attack by NO_2^+ ions in the HNO_3 solution under reflux, as shown previously.¹¹ All electrochemistry and single-molecule measurements presented in the main text were done on purified SWNTs.

To further ensure that the electrocatalytic activity of SWNTs is not due to impurities, we compared the electrocatalytic activity of SWNTs before and after purification. The electrocatalytic activity of purified SWNTs is higher than the unpurified ones (Figure S4C), supporting that the electrocatalysis of resazurin reduction is due to SWNTs.

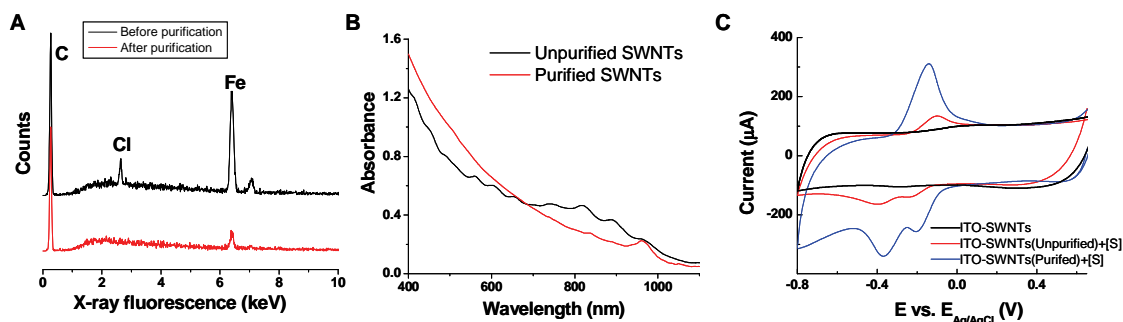


Figure S4. (A) EDX spectra of SWNTs before and after purification. The emission peaks of carbon, chlorine, and iron are labeled. (B) Absorption spectra of SWNTs before and after purification. The spectral features of metallic SWNTs in the $\sim 400\text{-}650$ nm region decrease relatively to those of semiconducting ones in the $\sim 650\text{-}1000$ nm region after purification. The sloping in the absorption spectra is due to particle scattering, as SWNTs exist as suspensions in the solution. (C) Cyclic voltammograms of $50\ \mu\text{M}$ resazurin in $50\ \text{mM}$ pH 7.3 phosphate buffer at the scan rate of $200\ \text{mV s}^{-1}$ using SWNTs-coated ITO electrode before and after purification of SWNTs. The background current is also shown in the absence of resazurin.

II.5. Test of electrocatalytic activity of Fe and Cu nanoparticles.

Based on the information from the company (Carbon Nanotechnologies Incorporated) and previous studies,¹² the SWNTs may contain residual Fe or Cu nanoparticle catalysts, although our EDX analysis only identified Fe as the significant metal residual (Figure S4A). To check directly if residual Fe, or Cu nanoparticles, could be responsible for the observed electrocatalytic activity of SWNTs, we performed cyclic voltammetry of resazurin and resorufin using Fe and Cu nanoparticle-coated ITO as working electrodes.

We prepared Fe nanoparticle through reduction of $\text{Fe}(\text{NO}_3)_2$ by NaBH_4 . Specifically, $100\ \text{mM}$ NaBH_4 solution was added drop-wise into a $10\ \text{mM}$ $\text{Fe}(\text{NO}_3)_3$ solution under stir to reduce Fe^{3+} to Fe. We then centrifuged the solution to obtain the nanoparticles as precipitates, which were washed several times with deionized water before drying in oven at 80°C . (Although the prepared Fe nanoparticle may get oxidized in air, they will be electro-reduced in situ in cyclic voltammetry measurements. Similar case for the Cu nanoparticles described below.) To make Fe-nanoparticle coated ITO electrode, we first dispersed $5\ \text{mg}$ Fe nanoparticles in $1\ \text{mL}$ ethanol solution and mixed

with 10 μL 5% Nafion solution. After 30-minute sonication, 20 μL of this solution was added onto the ITO electrode surface and dried. Using the Fe-nanoparticles-coated ITO as the working electrode and with just the buffer solution, the CVs show some redox processes of the Fe nanoparticles themselves (Figure S5A). In the presence of resazurin or resorufin, no catalytic currents were observed at all in the CVs (Figure S5A), indicating that Fe nanoparticles cannot mediate redox of resazurin or resorufin.

We prepared Cu nanoparticles via reduction of CuSO_4 by NaBH_4 . The procedures for the preparation of Cu nanoparticles and Cu-nanoparticle-coated ITO electrode are the same as those for Fe Nanoparticles described above. Using the Cu-nanoparticles-coated ITO as the working electrode and with just the buffer solution, the CVs show some redox processes of the Cu nanoparticles themselves (Figure S5B). In the presence of resazurin or resorufin, no changes were observed in the CVs (Figure S5B), indicating that Cu nanoparticles cannot mediate redox of resazurin or resorufin. We also performed CV using copper tape as the working electrode; the result shows that bulk Cu cannot mediate resazurin or resorufin redox, either.

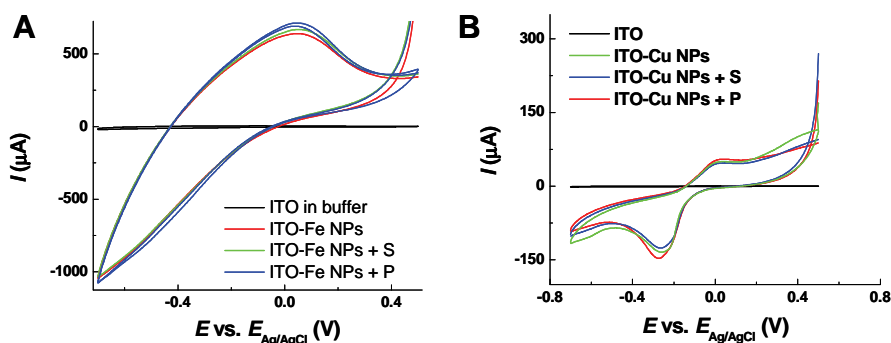


Figure S5. Cyclic voltammograms of 50 μM resazurin (S) and 50 μM resorufin (P) in 50 mM pH 7.3 phosphate buffer using Fe nanoparticle-coated ITO electrode (A) and Cu nanoparticle-coated ITO electrode (B). NPs: nanoparticles. All CVs at the scan rate 200 mV s^{-1} .

II.6. Electrochemistry of other carbon-based materials

We also studied the electrocatalytic properties of carbon black (Vulcan XC-72, Cabot Corporation) on ITO surface in mediating the redox of resazurin and resorufin. The cyclic voltammograms show that carbon black can also electrocatalyze the redox of resazurin and resorufin (Figure S6A), suggesting that this electrocatalytic activity is probably general to carbon-based materials.

Using the same amount of material loading on the ITO electrode, the peak currents in the CV using purified-SWNTs-coated ITO are larger than that of using carbon-black-coated ITO electrode (Figure S6B), indicating that SWNTs have higher electrocatalytic activity per unit mass than carbon black. Therefore, the observed electrocatalytic activity of purified SWNTs cannot be mainly due to the residual amorphous carbon or carbon particle impurities, as the amount of these impurities is very small in the purified SWNTs. If the electrocatalytic activity observed for the SWNTs

sample were mainly due to these residual carbon-based impurities, the activity of the SWNTs sample would be very small compared to pure carbon-black, which is not the case as shown in Figure S6B.

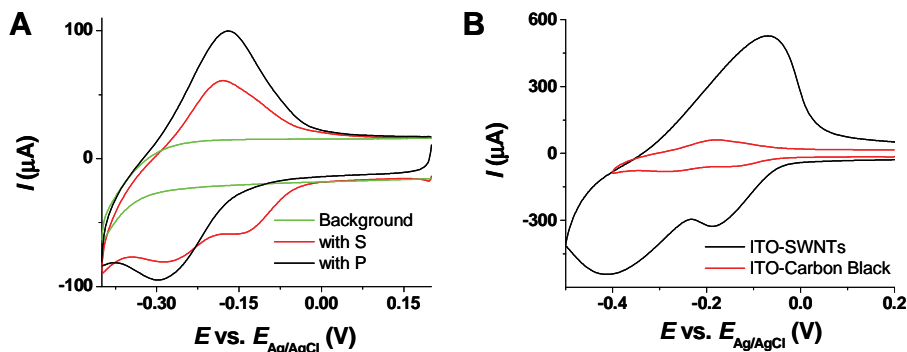


Figure S6. (A) Cyclic voltammograms of 50 μM resazurin and resorufin in 50 mM pH 7.3 phosphate buffer using carbon-black-coated ITO electrode. Scan rate: 200 mV s^{-1} . (B) Comparison of cyclic voltammograms of 50 μM resazurin using SWNTs-coated or carbon-black-coated ITO electrode at the same catalyst loading and 200 mV s^{-1} .

II.7. AFM measurements of surface dispersion of SWNTs

To probe if SWNTs can be dispersed well on the ITO surface, we used atomic force microscopy (AFM) to image the SWNTs deposited on a fused silica substrate. The AFM images show that SWNTs can be dispersed well on the surface by simple deposition of extensively sonicated, diluted SWNTs suspensions (Figure S7). Many single SWNTs are observed, but bundles of SWNTs are also present on the surface. The presence of bundles do not affect the observation of our single-molecule electrocatalysis experiments by SWNTs, as we observed reactions at localized reaction sites (Figures 2B and 3), each of which should belong to one SWNT.

Please note that in preparing the sample for AFM imaging, much larger amount of SWNTs were deposited onto the silica substrate to facilitate AFM imaging than the amount deposited in single-molecule electrocatalysis experiments. Moreover, the image in Figure S7 represents a denser region of SWNTs. In our single-molecule electrocatalysis experiment, the surface density of SWNTs is much lower.

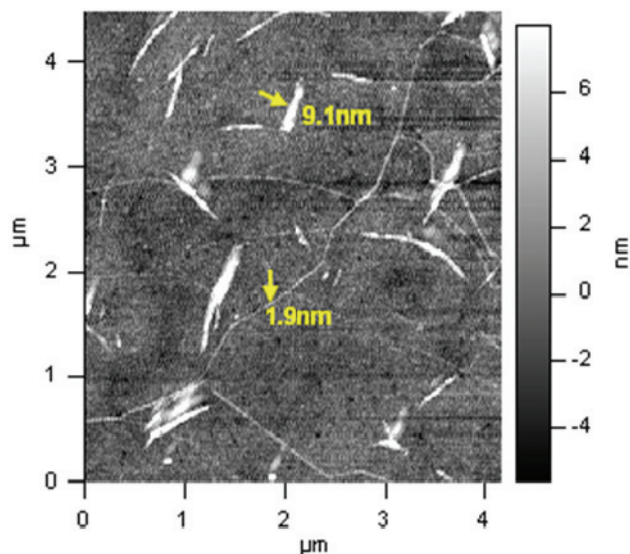


Figure S7. AFM image of SWNTs dispersed on a silica substrate. The numbers in yellow denotes the heights, i.e., the diameters, of the indicated SWNTs. Many individual SWNTs are apparent on the surface with heights of ~ 1 -2 nm. Bundles of SWNTs are also present with heights of a few nanometers.

II.8. Long segment of real-time single-reaction resolution trajectory of SWNT electrocatalysis

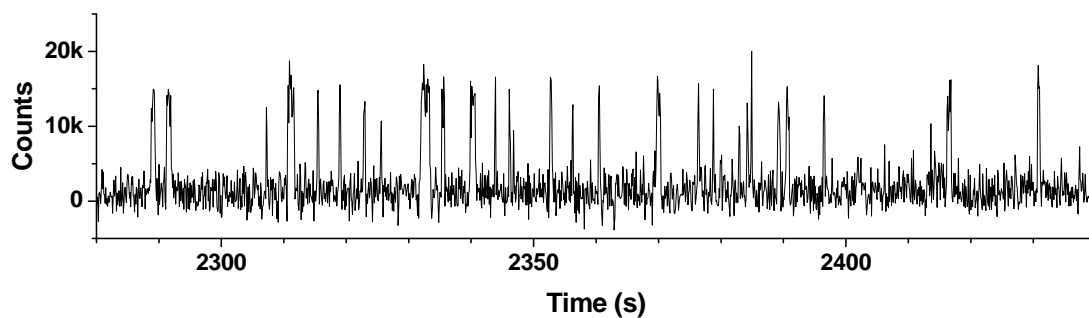


Figure S8. A longer segment of the electrocatalysis trajectory showing many more reaction events, derived from the same reaction site as in Figure 2C.

II.9. Additional data of super-resolution imaging of SWNT reactive sites

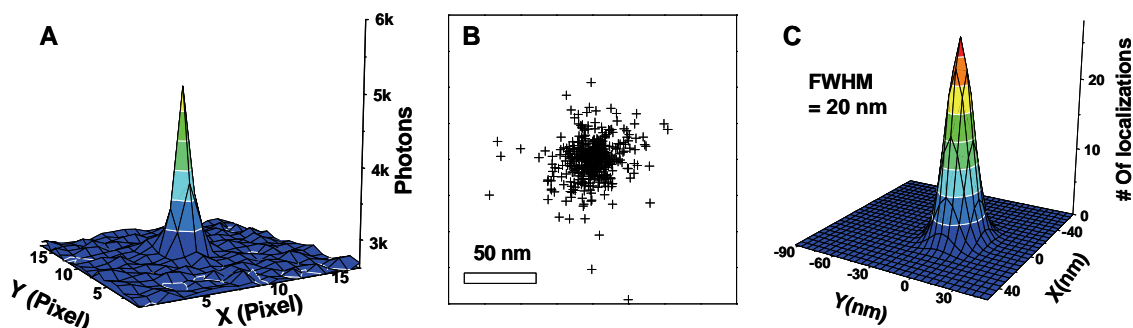


Figure S9. (A) Surface contour plot of the wide-field fluorescence image depicting the emission PSF of a resorufin molecule at a SWNT reactive site during a τ_{on} period. Pixel size = 267 nm. (B) Overlaid center localizations from 25 reactive sites. The center of mass of the localizations from each reactive site was used for alignment, as done in STORM imaging.⁵ (C) The two-dimensional Gaussian fitting to the two-dimension histogram of the localizations in (B). See Figure 3D for the two-dimensional histogram.

II.10. Resorufin photobleaching and blinking timescale determination

To probe if photobleaching or blinking of resorufin contributes to the distribution of τ_{on} in the single-molecule electrocatalysis trajectories of SWNTs, we directly measured the single-molecule fluorescence intensity trajectories of resorufin. We immobilized resorufin molecules in a polymethyl-methacrylate (PMMA) (Aldrich) film by spin-coating 20 μL of 50 pM solution of resorufin in PMMA in toluene onto a slide according to literature procedures.¹³ A ~ 10 μm water layer was then added on top of the PMMA film to provide an approximate aqueous environment. A coverslip was then used to sandwich the sample for measurements on our total internal reflection fluorescence microscope.

We excited resorufin with laser intensity of $\sim 13 \times 10^{-4}$ $\text{mW}/\mu\text{m}^2$, the same laser intensity used for single-molecule electrocatalysis experiments. Figure S10A is a typical fluorescence intensity trajectory of a resorufin molecule, which shows two blinking events and the eventual photobleaching. The average photobleaching time of ~ 350 resorufin molecules is ~ 17 s. Figure S10B gives the distribution of the photobleaching lifetimes of the resorufin molecules. It can be fitted by a single-exponential decay function with a time constant of ~ 13 s. Both the average photobleaching lifetime and the time constant from fitting the distribution are significantly larger than the average τ_{on} in our single-molecule electrocatalysis trajectories (about 0.1 – 0.5 s, Figures 2C and 5 in the text). Therefore, photobleaching does not contribute significantly to the distribution of τ_{on} in our single-molecule electrocatalysis experiments.

The distribution of the on-times between blinking events are shown in Figure S10B. The average on-time is ~ 5 s; fitting the distribution of the on-times with an exponential decay function gives a time constant of ~ 4.7 s; both times are much longer

than the average τ_{on} in our single-molecule electrocatalysis trajectories (Figures 2C and 5). Therefore, resorufin blinking does not contribute significantly to the τ_{on} distribution in our electrocatalysis experiments, either.

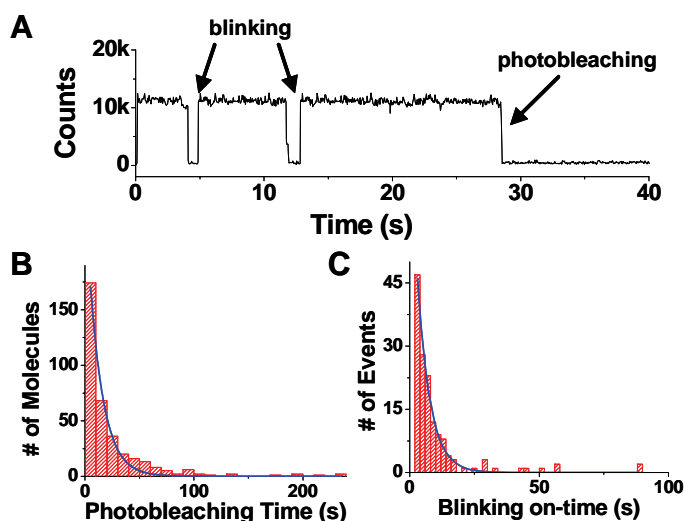


Figure S10. (A) A typical fluorescence intensity trajectory of a resorufin molecule showing blinking events and eventual photobleaching. (B) Distribution of lifetimes before photobleaching of individual resorufin molecules. Solid line is a single-exponential decay fit with a time constant of ~ 13 s. (C) Distribution of the blinking on-times of resorufin. Solid line is a single exponential decay fit with a time constant of ~ 4.7 s.

II.11. Kinetic mechanism of electrocatalysis and derivations of the single-molecule rate equations.

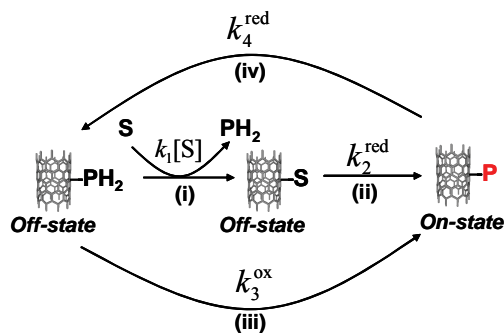
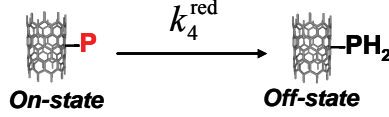


Figure S11. Kinetic mechanism of SWNT electrocatalysis as in Figure 5C.

The single-molecule electrocatalysis fluorescence trajectories of SWNTs such as that in Figure 2C clearly separate the electrocatalysis into two parts: the τ_{on} process and the τ_{off} process. Therefore, we can treat the single-molecule kinetics of τ_{on} and τ_{off} processes separately.^{8,14,15}

τ_{on} is the waiting time for **P** electroreduction to **PH₂**, after a **P** is formed at a reactive site. Based on the mechanism in Figure S11, the reaction that takes place during τ_{on} is reaction (iv), a simple one-step reaction:



For this simple one-step reaction, the probability density function $f_{\text{on}}(\tau)$ of the waiting time τ_{on} is:^{14,15}

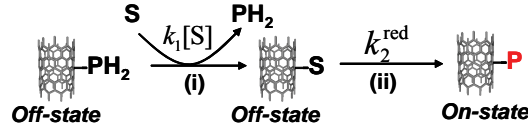
$$f_{\text{on}}(\tau) = k_4^{\text{red}} \exp(-k_4^{\text{red}} \tau) \quad (\text{S1})$$

And,

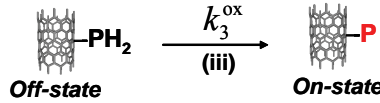
$$\langle \tau_{\text{on}} \rangle^{-1} = 1 / \int_0^{\infty} f_{\text{on}}(\tau) d\tau = k_4^{\text{red}} \quad (\text{S2})$$

This equation is given as Equation (1) in the text.

τ_{off} is the waiting time for **P** formation at a reactive site. Based on the mechanism in Figure S11, the reactions that take place during τ_{off} are either reactions (i) and (ii):



or reaction (iii):



The corresponding single-molecule rate equations are:

$$\frac{dP_{*-\text{PH}_2}(t)}{dt} = -(k_1^0 + k_3^{\text{ox}}) P_{*-\text{PH}_2}(t) \quad (\text{S3a})$$

$$\frac{dP_{*-\text{S}}(t)}{dt} = k_1^0 P_{*-\text{PH}_2}(t) - k_2^{\text{red}} P_{*-\text{S}}(t) \quad (\text{S3b})$$

$$\frac{dP_{*-\text{P}}(t)}{dt} = k_2^{\text{red}} P_{*-\text{S}}(t) + k_3^{\text{ox}} P_{*-\text{PH}_2}(t) \quad (\text{S3c})$$

where $k_1^0 = k_1[\text{S}]$, and $P_{*-\text{PH}_2}(t)$, $P_{*-\text{S}}(t)$, and $P_{*-\text{P}}(t)$ are the probabilities at time t that the SWNT reactive site has **PH₂**, **S**, and **P** bound, respectively. “*” here designates the reactive site on a SWNT. The initial conditions for solving the Equations S3a-c are:

$$P_{*-\text{PH}_2}(0) = 1, P_{*-\text{S}}(0) = P_{*-\text{P}}(0) = 0$$

with $t = 0$ being the onset of each off-time τ_{off} , and at any time t within τ_{off} , $P_{*-\text{PH}_2}(t) + P_{*-\text{S}}(t) + P_{*-\text{P}}(t) = 1$.

We can then consider the probability density $f_{\text{off}}(\tau)$ of the off-time τ_{off} . τ_{off} is the time required to finish reactions (i) and (ii), or the time required to finish reaction (iii). The probability for finding a particular τ is $f_{\text{off}}(\tau)\Delta\tau$, which is equal to probability of

switching to $*-\mathbf{P}$ state from either the $*-\mathbf{S}$ state or $*-\mathbf{PH}_2$ state between the time τ and $\tau+\Delta\tau$. This probability is $\Delta P_{*-p}(t)$, which equals $(k_2^{\text{red}} P_{*-S}(t) + k_3^{\text{ox}} P_{*-PH_2}(t))\Delta t$. Then $f_{\text{off}}(\tau)$ is:

$$f_{\text{off}}(\tau) = \frac{dP_{*-p}(t)}{dt} \Big|_{t=\tau} = k_2^{\text{red}} P_{*-S}(\tau) + k_3^{\text{ox}} P_{*-PH_2}(\tau).$$

Solving Equations S3a-c for $P_{*-PH_2}(\tau)$ and $P_{*-S}(\tau)$ with the initial conditions, we obtain:

$$f_{\text{off}}(\tau) = \frac{(k_2^{\text{red}} k_1^0 + k_3^{\text{ox}} a + k_3^{\text{ox}} b + k_3^{\text{ox}} k_2^{\text{red}}) e^{(b+a)\tau}}{2a} + \frac{(-k_2^{\text{red}} k_1^0 + k_3^{\text{ox}} a - k_3^{\text{ox}} b - k_3^{\text{ox}} k_2^{\text{red}}) e^{(b-a)\tau}}{2a} \quad (\text{S4})$$

with $a = \sqrt{\frac{1}{4}(k_1^0 + k_2^{\text{red}} + k_3^{\text{ox}})^2 - (k_2^{\text{red}} k_1^0 + k_2^{\text{red}} k_3^{\text{ox}})}$, and $b = -\frac{1}{2}(k_1^0 + k_2^{\text{red}} + k_3^{\text{ox}})$.

Then $\langle \tau_{\text{off}} \rangle^{-1}$, which represents the time-averaged \mathbf{P} formation rate at a single reactive site, is,

$$\langle \tau_{\text{off}} \rangle^{-1} = 1 / \int_0^{\infty} f_{\text{off}}(\tau) d\tau = \frac{k_2^{\text{red}} (k_3^{\text{ox}} + k_1[\text{S}])}{k_2^{\text{red}} + k_1[\text{S}]} \quad (\text{S5})$$

Equation S5 is given as Equation (2) in the main text. Consider the limiting conditions for $\langle \tau_{\text{off}} \rangle^{-1}$. When $[\text{S}] \rightarrow 0$,

$$\langle \tau_{\text{off}} \rangle_{[\text{S}] \rightarrow 0}^{-1} = k_3^{\text{ox}}$$

When $[\text{S}] \rightarrow \infty$,

$$\langle \tau_{\text{off}} \rangle_{[\text{S}] \rightarrow \infty}^{-1} = k_2^{\text{red}}$$

To give a physical interpretation of $[\text{S}]$ dependence of $\langle \tau_{\text{off}} \rangle^{-1}$, when $[\text{S}] \rightarrow 0$, the forward reaction of reaction (i) is extremely slow ($k_1[\text{S}] = 0$, Figure S11) and thus effectively shut down. Then the dominant process for \mathbf{P} formation during τ_{off} is reaction (iii), and the reaction rate is determined by k_3^{ox} , the rate constant for direct oxidation of \mathbf{PH}_2 to \mathbf{P} . When $[\text{S}] \rightarrow \infty$, the $*-\mathbf{PH}_2$ state will be immediately converted to the $*-\mathbf{S}$ state via reaction (i) due to the large value of $k_1[\text{S}]$; then the \mathbf{P} formation will dominantly come from the electro-reduction of $*-\mathbf{S}$ and the reaction rate is determined by k_2^{red} , the reaction (ii).

With different relative magnitudes between k_2^{red} and k_3^{ox} , Equation S5 predicts variable $[\text{S}]$ -dependence of $\langle \tau_{\text{off}} \rangle^{-1}$. 1) When $k_2^{\text{red}} > k_3^{\text{ox}}$, $\langle \tau_{\text{off}} \rangle^{-1}$ will increase with increasing $[\text{S}]$ and eventually saturate. 2) When $k_2^{\text{red}} < k_3^{\text{ox}}$, $\langle \tau_{\text{off}} \rangle^{-1}$ will decrease with increasing $[\text{S}]$ and flatten. Both of these behaviors have been observed in our single-molecule electrocatalysis experiments (Fig. 5B). Of course, there is a special third type: when $k_2^{\text{red}} = k_3^{\text{ox}}$, $\langle \tau_{\text{off}} \rangle^{-1}$ will be independent of $[\text{S}]$; this type of behavior was also observed, but not shown in the text.

Further discussions of the kinetic mechanism.

Reaction (i). This reaction is necessitated by the $[S]$ -dependence of $\langle \tau_{\text{off}} \rangle^{-1}$, which indicates the **S** must participate in the formation of **P**. This reaction is taken as irreversible, because the reverse reaction would require **PH₂**, whose concentration is extremely low in the reaction solution. Under our experimental conditions, as soon as **PH₂** leaves the SWNT reactive site, it will undergo fast diffusion and be carried away by the solution follow.

Reaction (ii). This **S** \rightarrow **P** electroreduction reaction is known to be irreversible (Figure 1).¹⁶

Reaction (iii). This **PH₂** \rightarrow **P** reaction is the reverse reaction of **P** \rightarrow **PH₂** (reaction (iv)). **P** \leftrightarrow **PH₂** redox is known to be reversible (Figure 1).¹⁶

II.12. Another possible but inapplicable mechanism of electrocatalysis.

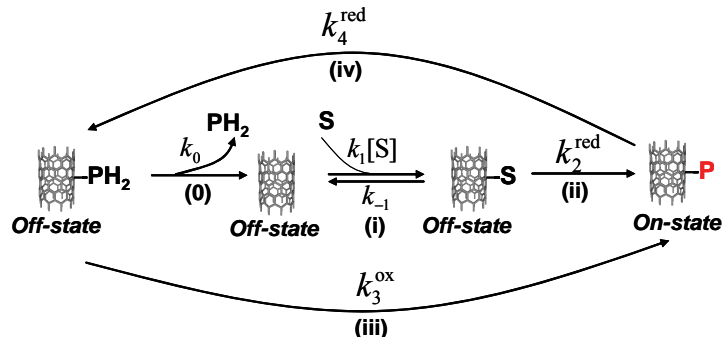
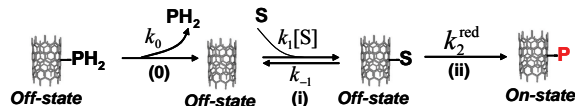


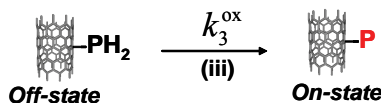
Figure S12. Alternative kinetic mechanism of SWNT electrocatalysis.

In this possible mechanism, the substitution reaction (reaction (i) in Figure S11) is broken into two steps: one the dissociation of **PH₂** from the reactive site (reaction (0) in Figure S12), which is taken to be irreversible, as $[PH_2]$ is extremely low in the reaction solution; and the other the binding of **S** to the reactive site (reaction (i) in Figure S12), which is taken to be reversible.

Using this mechanism, the τ_{on} process is the same as in the mechanism in Figure S11. $\langle \tau_{\text{on}} \rangle^{-1}$ follows Equation S2. The τ_{off} process is different and consists of the following parallel reactions:



and



The corresponding single-molecule rate equations are:

$$\frac{dP_{*-PH_2}(t)}{dt} = -(k_0 + k_3^{ox})P_{*-PH_2}(t) \quad (S6a)$$

$$\frac{dP_*(t)}{dt} = k_0P_{*-PH_2}(t) \quad (S6b)$$

$$\frac{dP_{*-S}(t)}{dt} = k_1^0P_*(t) - (k_{-1} + k_2^{red})P_{*-S}(t) \quad (S6c)$$

$$\frac{dP_{*-P}(t)}{dt} = k_2^{red}P_{*-S}(t) + k_3^{ox}P_{*-PH_2}(t) \quad (S6d)$$

where $k_1^0 = k_1[\mathbf{S}]$, and $P_{*-PH_2}(t)$, $P_*(t)$, $P_{*-S}(t)$ and $P_{*-P}(t)$ are the probabilities at time t that the SWNT reactive site has \mathbf{PH}_2 , nothing, \mathbf{S} , and \mathbf{P} bound, respectively. The initial conditions for solving the Equations S6a-d are:

$$P_{*-PH_2}(0) = 1, P_*(0) = P_{*-S}(0) = P_{*-P}(0) = 0$$

with $t = 0$ being the onset of each off-time τ_{off} , and at any time t within τ_{off} , $P_{*-PH_2}(t) + P_*(t) + P_{*-S}(t) + P_{*-P}(t) = 1$.

Similarly, we have $f_{off}(\tau) = \left. \frac{dP_{*-P}(t)}{dt} \right|_{t=\tau} = k_2^{red}P_{*-S}(\tau) + k_3^{ox}P_{*-PH_2}(\tau)$. Solve the Equations S6a-d for $P_{*-PH_2}(t)$ and $P_{*-S}(t)$, we can obtain $f_{off}(\tau)$, which is tediously complex and not presented here. Then,

$$\langle \tau_{off} \rangle^{-1} = 1 / \int_0^\infty \mathcal{G}_{off}(\tau) d\tau = \frac{k_0 k_1 [\mathbf{S}] k_2^{red} + k_2^{red} k_1 [\mathbf{S}] k_3^{ox}}{k_0 k_{-1} + k_2^{red} k_0 + k_0 k_1 [\mathbf{S}] + k_2^{red} k_1 [\mathbf{S}]} \quad (S7)$$

Considering the limiting conditions, when $[\mathbf{S}] \rightarrow 0$;

$$\langle \tau_{off} \rangle_{[\mathbf{S}] \rightarrow 0}^{-1} = 0$$

when $[\mathbf{S}] \rightarrow \infty$,

$$\langle \tau_{off} \rangle_{[\mathbf{S}] \rightarrow \infty}^{-1} = \frac{k_0 k_2^{red} + k_2^{red} k_3^{ox}}{k_0 + k_2^{red}}$$

Therefore, with decreasing $[\mathbf{S}]$, this mechanism would predict that $\langle \tau_{off} \rangle^{-1}$ decreases and approaches zero. This prediction is inconsistent with the observed $[\mathbf{S}]$ -dependence of $\langle \tau_{off} \rangle^{-1}$ at -0.1V (Figure 5B, and Figure 6A, lower panel). ***This mechanism is thus inapplicable for the SWNT electrocatalysis studied here.***

To give a physical interpretation of the limiting value of $\langle \tau_{off} \rangle_{[\mathbf{S}] \rightarrow 0}^{-1}$. The τ_{off} process in this mechanism has two parallel pathways: one consists of reactions (0), (i), and (ii); and the other consists of reaction (iii) only. Both pathways occur regardless of $[\mathbf{S}]$. Even at $[\mathbf{S}] \rightarrow 0$, the first pathway still occurs, because reaction (0) has non-zero rate (k_0); however, at this condition, the forward reaction (i) is extremely slow ($k_1[\mathbf{S}] \rightarrow 0$), leading to infinite long τ_{off} 's. This results in $\langle \tau_{off} \rangle_{[\mathbf{S}] \rightarrow 0}^{-1} = 0$.

II.13. Estimate of diffusion-limited reaction rate at a single reaction site of SWNTs.

To estimate the mass-transport (i.e., diffusion) limited steady-state reaction rate at a single reaction site of SWNTs, we approximated each reaction site as an ultra-small hemispherical electrode with a radius of 0.5 nm (the diameter of the SWNTs is about 1-2 nm). The diffusion-limited steady-state current density, j_{ss} , is then:^{17,18}

$$j_{ss} = \frac{nFDc_0}{r_0}$$

where n is the number of the electrons per reaction, F is the Faraday constant (96485 C), D is the diffusion constant of the reactant, c_0 is the bulk concentration of the reactant, and r_0 is the radius of the electrode. At a low reactant concentration, e.g., 0.01 μM , using a typical diffusion constant $D = 10^{-6} \text{ cm}^2\text{s}^{-1}$ for small molecules in water,^{18,19} and $n = 4$, j_{ss} is $8 \times 10^{-5} \text{ A cm}^{-2}$.

In our single-molecule electrocatalysis experiments, at 0.01 μM resazurin, the typical turnover rate observed is about $1/30 \text{ s}^{-1}$ at a single reaction site. With $n = 4$ for the total 4-electron reduction of resazurin to dihydroresorufin, the corresponding current density is $\sim 7 \times 10^{-7} \text{ A cm}^{-2}$ with the approximation of a hemisphere electrode. This is two orders of magnitudes smaller than the expected diffusion-limited current density ($8 \times 10^{-5} \text{ A cm}^{-2}$, above). Therefore, in our single-molecule electrocatalysis experiments, the measured reaction rate is not limited by diffusion (i.e., mass transport), but by the electrocatalytic charge transfer reactions.

References

1. Huang, H., Maruyama, R., Noda, K., Kajiura, H. & Kadono, K. Preferential destruction of metallic single-walled carbon nanotubes by laser irradiation. *J. Phys. Chem. B* **106**, 7316-7320 (2006).
2. Hu, H., Zhao, B., Itkis, M. E. & Haddon, R. C. Nitric acid purification of single-walled carbon nanotubes. *J. Phys. Chem. B* **107**, 13838-13842 (2003).
3. Yu, A., Bekyarova, E., Itkis, M. E., Fakhruddinov, D., Webster, R. & Haddon, R. C. Application of centrifugation to the large-scale purification of electric arc-produced single-walled carbon nanotubes. *J. Am. Chem. Soc.* **128**, 9902 -9908 (2006).
4. Rust, M. J., Bates, M. & Zhuang, X. Sub-diffraction-limit imaging by stochastic optical reconstruction microscopy (storm). *Nature Methods* **3**, 793-796 (2006).
5. Bates, M., Huang, B., Dempsey, G. T. & Zhuang, X. Multicolor super-resolution imaging with photo-switchable fluorescent probes. *Science* **317**, 1749-1753 (2007).
6. Thompson, R. E., Larson, D. R. & Webb, W. W. Precise nanometer localization analysis for individual fluorescent probes. *Biophys. J.* **82**, 2775-2783 (2002).
7. Yildiz, A., Forkey, J. N., McKinney, S. A., Ha, T., Goldman, Y. E. & Selvin, P. R. Myosin v walks hand-over-hand: Single fluorophore imaging with 1.5-nm localization. *Science* **300**, 2061-2065 (2003).

8. Xu, W., Kong, J. S., Yeh, Y.-T. E. & Chen, P. Single-molecule nanocatalysis reveals heterogeneous reaction pathways and catalytic dynamics. *Nature Mater.* **7**, 992-996 (2008).
9. Jurkschat, K., Ji, X., Crossley, A., Compton, R. G. & Banks, C. E. Super-washing does not leave single walled carbon nanotubes iron-free. *Analyst*, 2007, 132, 21-23. *Analyst* **132**, 21-23 (2007).
10. Strano, M. S. et al. Electronic structure control of single-walled carbon nanotube functionalization. *Science* **301**, 1519-1522 (2003).
11. Yang, C.-M. et al. Selective removal of metallic single-walled carbon nanotubes with small diameters by using nitric and sulfuric acids. *J. Phys. Chem. B* **109**, 19242-19248 (2005).
12. Wang, J. S., Wai, C. M., Shimizu, K., Cheng, F., Boeckl, J. J., Maruyama, B. & Brown, G. Purification of single-walled carbon nanotubes using a supercritical fluid extraction method. *J. Phys. Chem. C* **111**, 13007-13012 (2007).
13. Macklin, J. J., Trautman, J. K., Harris, T. D. & Brus, L. E. Imaging and time-resolved spectroscopy of single molecules at an interface. *Science* **272**, 255-258 (1996).
14. Xie, X. S. Single-molecule approach to enzymology. *Single Mol.* **2**, 229-236 (2001).
15. Xu, W., Kong, J. S. & Chen, P. Single-molecule kinetic theory of heterogeneous and enzyme catalysis. *J. Phys. Chem. C* **113**, 2393-2404 (2009).
16. Twigg, R. S. Oxidation-reduction aspects of resazurin. *Nature* **155**, 401-402 (1945).
17. Bard, A. J. & Faulkner, L. R. *Electrochemical methods: Fundamentals and applications* (John Wiley & Sons, Inc., 2000).
18. Meier, J., Friedrich, K. A. & Stimming, U. Novel method for the investigation of single nanoparticle reactivity. *Faraday Discuss.* **121**, 365-372 (2002).
19. Lide, D. R. (ed.) *Crc handbook of chemistry and physics* (CRC Press, Inc., Boca Raton, 1995).